

1 **Off-resonance saturation as an MRI method to quantify ferritin-**
2 **bound iron in the post-mortem brain**

3 Lucia Bossoni¹, Ingrid Hegeman-Kleinn², Sjoerd G. van Duinen², Lena H. P. Vroegindewij³,
4 Janneke G. Langendonk³, Lydiane Hirschler¹, Andrew Webb¹, Louise van der Weerd¹

5 ¹*C. J. Gorter Center for High field MRI, Department of Radiology, Leiden University Medical Center,*
6 *Leiden, The Netherlands.*

7 ²*Department of Pathology, Leiden University Medical Center, Leiden, The Netherlands*

8 ³*Department of Internal Medicine, Center for Lysosomal and Metabolic Diseases, Porphyria Center*
9 *Rotterdam, Erasmus University Medical Center, Rotterdam, The Netherlands.*

10

11 **Running Title:** Off-resonance saturation to image ferritin iron

12

13

14 **Corresponding author:**

15 Lucia Bossoni, PhD

16 Leiden University Medical Center

17 PO Box 9600, 2300 RC Leiden, The Netherlands

18 T. +31 71 526 44 77 | E. l.bossoni@lumc.nl

19

20 **Word Count:** 4655

21

22

23

24

25

26

27

28

1 **Abstract**

2 **Purpose**

3 To employ an Off-Resonance Saturation (ORS) method to measure the ferritin-bound iron pool,
4 which is an endogenous contrast agent which can give information on cellular iron status.

5 **Methods**

6 An ORS acquisition protocol was implemented on a 7T preclinical scanner and the contrast maps
7 were fitted to an established analytical model. The method was validated by correlation and Bland-
8 Altman analysis on a ferritin-containing phantom. Ferritin-iron maps were obtained from post-mortem
9 tissue of patients with neurological diseases characterized by brain iron accumulation, i. e.
10 Alzheimer's disease, Huntington's disease and aceruloplasminemia, and validated with histology.
11 Transverse relaxation rate and magnetic susceptibility values were also obtained for comparison.

12 **Results**

13 In post-mortem tissue, the ferritin-iron contrast strongly co-localizes with histological iron staining, in
14 all the cases. Quantitative iron values obtained via the ORS method are in agreement with literature.

15 **Conclusions**

16 Off-resonance saturation is an effective way to detect iron in grey matter structures, while mitigating
17 for the presence of myelin. If a reference region with little iron is available in the tissue, the method
18 can produce quantitative iron maps. This method is applicable in the study of brain diseases
19 characterized by brain iron accumulation and complement existing iron-sensitive parametric methods.

20

21

22 **Keywords** Iron, post-mortem MRI, ferritin, neurodegenerative diseases

23

24

25

26

27

1 Introduction

2 Physiological iron is distributed heterogeneously within the brain, with the structures richest in iron
3 being localized within the basal ganglia¹. The distribution of iron throughout the brain is likely related
4 to its fundamental biological processes, which involve oxygen transport, DNA synthesis, and
5 mitochondrial respiration². In contrast, the dysregulation of iron homeostasis is associated with
6 neurotoxicity via the formation of reactive oxygen species (ROS)²⁻⁶, lipid peroxidation⁷, and
7 ferroptosis⁸, a form of cell death characterized by phospholipid oxidation⁹. Iron is also thought to
8 trigger inflammation which can, in turn, lead to additional cellular iron release¹⁰.

9 Brain iron accumulation is a common phenomenon of several neurodegenerative diseases, despite
10 their different pathological hallmarks. Examples are Alzheimer's disease^{2,11}, Huntington's disease^{2,4,12},
11 and the neurodegeneration with brain iron accumulation (NBIA) group of disorders of which
12 aceruloplasminemia (ACP) is a rare phenotype¹³.

13 One of the primary cytoplasmic proteins responsible for intra- and extracellular iron storage is
14 ferritin¹⁴. Ferritin is composed of a 24-subunit shell (apoferritin) which plays three important roles in
15 iron regulation: it binds cytoplasmic Fe²⁺; it oxidizes Fe²⁺ into Fe³⁺ (as antioxidant protection); and it
16 stores iron in the form of a biocompatible nano-mineral¹⁵, ferrihydrite, or a mixture of ferrihydrite and
17 other minerals^{16,17}. Since the core of ferritin can bind up to ~5000 iron atoms, the nanoparticle's
18 saturated magnetic moment can reach ~300 μ_B ¹⁸. Ferritin-bound iron levels constitute ~ 80% of total
19 non-heme iron¹⁹ and therefore ferritin is commonly used as a reporter of tissue iron status. Although
20 ferritin-bound iron is unlikely to contribute directly to oxidative stress, its levels are related to the
21 labile iron pool^{20,21}, which is implicated in neurotoxicity.

22 MRI is very sensitive to the magnetic field perturbation caused by iron ions and iron nanoparticles
23 which have superparamagnetic properties. In the presence of iron, diffusing water molecules probe a
24 broad distribution of magnetic fields. Consequently, a time-dependent phase is accumulated, leading
25 to reduced T₂ and T₂^{*} relaxation times²²⁻²⁴. Ferritin-bound iron is the (physiological) iron form having
26 the largest effect on the MRI signal¹⁹ due to its large susceptibility and abundance. The most sensitive
27 MR methods for the detection of iron are the Field Dependent Transverse Relaxation Rate Increase
28 (FDRI)²⁵⁻²⁷, R₂^{*} and R₂ mapping^{28,29}, and Quantitative Susceptibility Mapping (QSM)³⁰. Although
29 quantitative maps of transverse relaxation rates and tissue magnetic susceptibility have already shown
30 benefits in the clinic^{22,31}, these parameter are also influenced by myelin content³²⁻³⁴, fiber
31 orientation³⁵, tissue microstructure³⁶, neuronal loss²⁹ and iron aggregation^{37,38}. Additionally, QSM
32 reconstructions can be affected by the non-local nature of the inverse problem that relates magnetic
33 field perturbation to magnetic susceptibility, and this impairs quantitative analysis.

34

1 In this work, we show how an off-resonance saturation (ORS) method, earlier introduced for the
2 detection of iron-oxide contrast agents^{39,40}, can be employed to assess ferritin-bound iron levels in the
3 post-mortem brain and overcome some of the limitations of conventional mapping methods.

4 We validated the method in a brain phantom, and we employed it to characterize the ferritin-bound
5 iron levels in post-mortem material obtained from three patients affected by neurological diseases
6 associated with increased brain iron. We assessed the ferritin-bound iron maps against QSM and R_2^*
7 maps, and histopathological staining for ferric iron, ferritin and myelin.

8 **Methods**

9 **Tissue selection and phantom preparation**

10 A ferritin-agar phantom was prepared by adding horse spleen ferritin (Sigma, ref. F4503) to a 1.5%
11 agar solution. Phantoms with different iron concentrations were prepared: 0 mM, 1.3 mM, 4.0 mM,
12 7.0 mM, 10.3 mM and 15.1 mM. The iron concentration was estimated by multiplying the ferritin
13 concentration by the average loading of the protein i.e. 2500 iron/ferritin⁴¹.

14
15 Formalin-fixed tissue blocks extracted from three diseased brains were studied. Brain material from a
16 patient with Huntington's disease (HD), a patient with Alzheimer's disease (AD) and a patient with
17 aceruloplasminemia (ACP) was obtained from the Pathology department of the LUMC, the
18 Netherlands Brain Bank, and the Erasmus Medical Center, respectively. Patient's informed consent
19 was obtained from each respective brain bank. For each case, a disease-relevant area was chosen: the
20 striatum for the HD case; the striatum and the globus pallidus for the ACP case; and the middle
21 temporal gyrus for the AD case. The tissue blocks were rehydrated in phosphate buffered solution
22 (PBS) for 24 hours prior to the scan, to partially restore transverse relaxation times. Subsequently, the
23 tissue was scanned in a hydrogen-free solution (Fomblin® LC08, Solvay).

24

25 **MRI data acquisition**

26 MRI data were acquired on a 7T preclinical scanner (Bruker Biospin, Ettlingen, Germany) using a 38
27 mm linear birdcage transmit-receive coil (T10327V3) with eight legs.

28 To compare the iron maps obtained with ORS to standard QSM and R_2^* maps, R_2^* -weighted images
29 were acquired using a 3D multiple gradient echo (MGE) sequence. The echo time (TE) was optimized
30 for the tissue block under study since the transverse relaxation (and iron load) largely varies per
31 region and disease. The acquisition parameters are summarized in Table 1.

32

1 ORS images were derived from 2D steady state free precession (SSFP) images (FISP-FID) with
2 TE/TR=3/6ms; inter-scan delay TR =2 s; FA= 10 degrees. A ‘control’ magnitude image (M_{control}),
3 without saturation pulses, was also acquired. Saturated images (M_{sat}) were produced by a saturation
4 module consisting of six hyperbolic secant pulses of bandwidth 500 Hz ($B_1=1.36 \mu\text{T}$), followed by a
5 spoiler gradient of 3 ms duration. The off-resonance saturation pulses were phase-cycled to improve
6 the spoiling. A list of M_{sat} was obtained upon varying the frequency of the off-resonance pulse.
7 Details of the off-resonance acquisition are reported in Table 2.

8 Raw data acquired in this study are freely available at the link:
9 <http://dx.doi.org/10.17632/nkznjnwppw.1>

10

11

12 MRI Data Processing

13 MGE-magnitude images were fitted on a pixel-by-pixel basis to a mono-exponential decay function²³,
14 after ruling out the presence of multi-components, using the Levenberg–Marquardt curve-fitting
15 algorithm to derive the transverse relaxation rate R_2^* . The noise floor was reached in the last 2 or so
16 echoes in some regions of the tissue (ACP) containing extremely high iron accumulation but did not
17 affect the overall fitting quality. To more accurately fit the data, we excluded the pixels with
18 intensities at the noise level.

19 Susceptibility values (χ) were obtained from the phase images with the STI-Suite software (version
20 2.2). Phase unwrapping of the measured phase images and removal of the background field were done
21 with iHARPERELLA⁴², while magnetic susceptibility estimation and streaking artifact correction
22 were performed with the ‘iLSQR’ algorithm⁴³. Raw susceptibility values are reported, as no reference
23 region was available in these small tissue samples.

24

25 Figure 1 illustrates the pipeline of the ORS analysis. ORS images (M_{ors}) were obtained from the
26 subtraction: $M_{\text{ors}} = M_{\text{control}} - M_{\text{sat}}$. Contrast (C) maps were obtained by subtracting the mean intensity
27 of M_{ors} in a region of reference (ROR) from the M_{ors} ⁴⁰. Under the assumption that the ROR contains
28 no iron, the contrast (C) can be written as the product of the fraction of protons (ϕ) saturated by the
29 ORS pulses and the intensity of the control image ($C=M_{\text{control}} \phi$). In our work, only positive frequency
30 offsets were chosen, to exclude Nuclear Overhauser Effects (NOE)-related artifacts⁴⁴ and to speed up
31 the acquisition. The saturated fraction of protons, as derived by Delangre *et al.*⁴⁰, is given by:

32

$$33 \quad \phi = \frac{1}{\pi} \left| \arctg(a(v_0 - \delta v + \Delta v/2)) - \arctg(a(v_0 - \delta v - \Delta v/2)) \right| \quad [1]$$

1 Where $a = \frac{3\sqrt{3}v_{mat}^{-1}}{2\pi\gamma[Fe]_{Beq}} = \frac{\alpha}{[Fe]_{Beq}}$, γ is expressed in MHz/T, $B_{eq} = \frac{\mu Ms}{3}$ is the stray field (in Tesla) at
2 the equator of a nanoparticle with saturation magnetization M_s , $[Fe]$ is the iron concentration (in
3 mM), and v_{mat} is the molar volume of ferrihydrite⁴⁵ and equal to $5.4 \times 10^{-6} \text{ m}^3/\text{mol} = 5.4 \times 10^{-6} \text{ mM}^{-1}$, and
4 $\alpha = 3.6 \times 10^{-3} \text{ T (Hz mM)}^{-1}$ (See Supplementary material for further details). A frequency offset ($\delta\nu$)
5 was added to account for resonance frequency shifts. Since $N=6$ saturation pulses were used to
6 enhance the saturation⁴⁶, the final expression for the contrast becomes:
7 $C(\nu_0) = N M_{control} \varphi(\nu_0 + off)$ [2]

8 $M_{control}$ is weighted by the proton density, relaxation times, and flip angle⁴⁷. The offset (*off*) term in the
9 equation above was introduced to account for residual MT effects and imperfect saturation. Finally,
10 the contrast map was fitted to equation [2] to derive the iron concentration, with the equatorial field as
11 a fixed parameter. The agreement between the fitted iron concentration and the known iron
12 concentration was assessed with correlative and Bland-Altman analyses.

13

14 **Histopathological validation**

15 The same tissue blocks used for MRI were employed for histology. Tissue blocks were embedded in
16 paraffin and sliced with a microtome into 5 μm and 20 μm thick sections. The 20 μm sections were
17 employed for non-heme iron detection (Meguro staining), according to Van Duijn *et al.*⁴⁸. After
18 deparaffinization, the tissue sections were incubated for 80 min in 1% potassium ferro-cyanide,
19 washed, followed by 100 min incubation in methanol with 0.01M NaN_3 and 0.3% H_2O_2 .
20 Subsequently, sections were washed with 0.1M phosphate buffer followed by 80 min incubation in a
21 solution containing 0.025% 3',3'-diaminobenzidine- tetrahydrochloride (DAB, Sigma-Aldrich) and
22 0.005% H_2O_2 in 0.1M phosphate buffer. The reaction was stopped by washing with tap water. The 5
23 μm slices were used for additional staining: non-heme (mostly trivalent) iron was detected with Perl's
24 Prussian blue (Merck 1.04984.0100); and immunohistochemical detection of myelin was done with
25 anti-myelin PLP antibody (Bio-Rad, MCA 839G) with second antibody Rb-aMs/biotin (DAKO) for
26 1h at room temperature, followed by ABC (avidin-biotin-complex/HRP, ABC Elite Kit, Vector) for
27 30 min at room temperature. Immunohistochemical detection of ferritin was done with ferritin
28 antibody (Bethyl A80-140, dilution 1:1000, overnight incubation at room temperature), with as
29 second step antigoat/biotin (Bethyl A50-204B, dilution:1:1000, 1h incubation at room temperature),
30 followed by ABC incubation for 30 min at room temperature. After the ABC treatment, the tissue was
31 rinsed three times with phosphate buffered saline and incubated in 0.05% DAB (Sigma-Aldrich) with
32 15 μl 30% H_2O_2 /100ml for 5-10 minutes. After rinsing several times with demineralized water, the
33 slices were counterstained for 30 s with Harris haematoxylin and washed for 5-10 mins with tap water.
34 Finally, the tissue sections were dehydrated with ethanol 70%, 96%, 100%, and xylene.

35

1 **Correlation between histology and ORS imaging**

2 To quantify the degree of agreement between the histological staining for iron with the ferritin-bound
3 iron concentration derived from the ORS method, oval regions of interest (ROI, N=30) were drawn in
4 the grey matter regions of the ferritin-bound iron maps and ORS maps. The iron staining image was
5 manually co-registered (affine transformation) to the MRI maps with the TrackEM2 plugin in ImageJ.
6 The registered image stack was converted to an 8-bit greyscale image. Oval ROIs were carefully
7 drawn and propagated between the iron histological map and the MRI map with the ROI manager
8 tool. Mean grey values from the predefined ROIs were quantified³², after inspecting for the precise
9 placement of the ROIs. Pearson's correlation coefficient (ρ) of the association between histological
10 staining intensity and the ferritin-bound iron map was calculated per case.

11

12 **Results**

13 **Validation on ferritin phantom**

14 Figure 2 shows the iron map obtained for the ferritin-loaded phantom and the ROI analysis on the
15 sample's compartments. The region of reference (ROR) was drawn in the middle of the phantom
16 containing only agar (Figure 1). The best-fitting results were obtained when fixing $B_{eq}=1$ mT, which
17 is very close to the theoretical value for ferritin (see Supplementary Information). The fitted iron
18 value agrees well with the nominal iron concentration, as assessed by the correlative plot in Figure
19 2C. Furthermore, the agreement between the iron concentration derived from the ORS map and the
20 nominal iron concentrations was assessed by Bland-Altman analysis (Figure 2D)^{49,50}, considering the
21 latter parameter as the reference value. No data fell outside of the limits of agreement and no
22 systematic bias was detected, at the 5% level of significance.

23

24 **Application to post-mortem material**

25 Figure 3 shows the results obtained for the middle temporal gyrus of the AD case. A comparison is
26 shown between the MRI parametric maps, i.e. R_2^* , QSM and the ORS-based ferritin-bound iron map
27 (termed $[Fe]_{ORS}$ map in the rest of the manuscript) and histology, i.e. myelin, iron and ferritin.
28 Elevated R_2^* levels are seen in the myelin-rich white matter and in the more superficial cortical layers.
29 In the QSM map, negative susceptibility is predominantly detected in the white matter. The $[Fe]_{ORS}$
30 map shows a strong localization of the iron in the cortex and (partially) in the white matter, thus
31 largely mirroring the QSM paramagnetic contrast and the histological staining of iron and ferritin
32 (protein), while it appears poorly correlated to the myelin histological staining. Across all tissue
33 blocks, the Perl's staining was considerably weaker than then Meguro staining, as earlier reported^{148,51},

1 and correlated less with the ferritin map, therefore our quantitative analysis was based on the Meguro
2 staining for iron, only.

3
4 The tissue block containing the striatum of the HD case (Figure 4) shows high R_2^* primarily in the
5 putamen (PU), some connecting fibers of the internal capsule (IC), and a thin stripe of the atrophied
6 caudate nucleus (CN). The susceptibility map looks heterogeneous, but with an overall positive
7 susceptibility in the PU and CN. The IC shows a characteristic striped appearance of alternating
8 positive and negative susceptibility. The $[Fe]_{ORS}$ map shows a localized increase of iron in the PU, a
9 thin stripe of the CN and of the external capsule. This map mirrors the iron staining, with the
10 exception of the external capsule and some connecting fibers of the internal capsule, which show no
11 contrast in the $[Fe]_{ORS}$ map, probably due to partial volume effects. The histological staining for
12 ferritin, iron and the $[Fe]_{ORS}$ map are largely opposite to the myelin-positive regions, which display
13 negative susceptibility in the QSM map. Note that the $[Fe]_{ORS}$ map shows iron contrast in a substantial
14 part of the external capsule, possibly due to iron in myelin.

15
16 Finally, the tissue block obtained from the ACP patient (Figure 5) shows high R_2^* in the putamen,
17 some connecting fibers of the internal capsule, the caudate nucleus and the globus pallidus ($R_2^* \sim 0.3$ -
18 0.6 ms^{-1}), similarly to the HD case. The QSM map is relatively smooth in the white matter regions,
19 while the grey matter is heterogeneous and presents a ‘patchy’ appearance (also observed in the MGE
20 images) which hinders quantitative analysis. The $[Fe]_{ORS}$ map on this tissue block shows diffuse iron
21 across both white and grey matter structures, except for the superior part of the internal capsule,
22 where the ROR was drawn. The histological iron staining (Meguro) appears very intense across the
23 whole slice, with a slightly higher intensity in the caudate nucleus and the globus pallidus, which is
24 also captured by the $[Fe]_{ORS}$ map. In contrast to the previous cases, the ferritin staining is rather weak
25 across the whole slice, as discussed below. Additional histological results on all the tissue blocks are
26 found in the Supplementary material (Figures S2-S5).

27

28 **Discussion:**

29 In this work we demonstrate how a method based on diffusion-mediated off-resonance saturation
30 (ORS)³⁹ can detect ferritin-bound iron concentrations from post-mortem brain material of an
31 Alzheimer’s (AD), Huntington’s (HD) and aceruloplasminemia (ACP) patient. This method can be
32 translated in vivo to evaluate tissue iron load and therapeutic efficacy on a pathophysiological level.

33 Water molecules diffusing around iron particles can be selectively excited by ORS pulses, based on
34 the correspondence between frequency offset and distance from the nanoparticle: the larger the
35 frequency offset, the closer the protons are to the dipolar-field source. It has been shown that the

1 positive contrast obtained by this method is distinct from, and can be observed also in the presence of,
2 MT effects³⁹. Although the ORS-method was originally introduced to quantify/detect
3 superparamagnetic iron-oxide nanoparticles (SPION), here we show that ORS can also be employed
4 to assess the presence and the concentration of ferritin-bound iron, by virtue of the super-
5 paramagnetic properties of the protein and its high concentration across the brain. Our results on the
6 agarose phantom show good agreement between nominal and fitted iron concentrations and support
7 the use of the method for iron quantification.

8 Visual comparison between the parametric MRI maps acquired in this study shows some advantages
9 of the ORS method: i) iron load appears highly localized in specific brain regions (mainly the gray
10 matter); ii) the white matter structures, which are highly myelinated, are predominantly masked out in
11 the $[\text{Fe}]_{\text{ORS}}$ maps, except for the ACP tissue where iron appears largely diffuse throughout the whole
12 slice; iii) the $[\text{Fe}]_{\text{ORS}}$ map largely mirrors the QSM map, when the latter is free from artefacts; iv) the
13 strength of the association between the $[\text{Fe}]_{\text{ORS}}$ maps and the iron staining was moderately high in all
14 cases ($\rho > 0.5$), and independent on the disease type.

15

16 The appearance of the ferritin-bound iron map in the tissue block obtained from the AD patient
17 suggests that, when looking at the temporal lobe, iron preferentially accumulates in the cortical grey
18 matter. This is in agreement with previous R_2^* ^{52,53} and QSM studies⁵⁴ reporting increased cortical iron
19 levels in patients with AD or mild cognitive impairment, which was associated with AD pathological
20 hallmarks, and an increased risk of cognitive decline. Magnetometry studies carried out on both
21 sporadic and genetic types of AD have also found that ferritin-bound iron is more abundant in the AD
22 group than in age- and gender-matched healthy controls^{55,56}.

23 Previous analytical studies have detected significant increase in the *total* iron content of the temporal
24 lobe of AD patients with respect to controls^{57,58}. However, the absolute iron concentrations ranged
25 from ~30 ng/mg⁵⁸ to 120 ng/mg (wet weight)⁵⁹, since age, gender, disease state and technique
26 sensitivity can impact the measured iron values. The highest cortical ferritin-bound iron
27 concentrations detected in our tissue block were 1.37 ± 0.25 mM (mean \pm sd), corresponding to 76.45
28 ± 13.95 ng/mg, which is in agreement with the estimate of ferritin-bound iron by magnetometry in the
29 AD temporal cortex⁵⁶, after correcting for dry weight mass-loss.

30

31 The ferritin-bound iron map of the tissue block from the HD patient shows an increase of iron in the
32 putamen and part of the atrophic caudate nucleus. Alterations in brain iron metabolism with increased
33 iron accumulation have been previously identified by MRI in the striatal nuclei of patients with
34 Huntington's disease^{26,60}. Iron accumulation in these structures seems to occur early on during the
35 disease process⁶¹, suggesting a key role of iron in the initiation and progression of the disease¹¹. In
36 fact, in vivo MRI studies at both 3T and 7T have shown that iron accumulation⁶² is associated with

1 tissue atrophy of basal ganglia structures and is already present in the premanifest phase of HD^{61,63,64}.
2 Our mean fitted iron concentration in the putamen was 4.66 ± 1.35 mM, equivalent to 260.0 ± 75.33
3 ng/mg, which agrees well with iron concentrations measured by inductively coupled mass
4 spectrometry¹².

5 Finally, the ferritin-bound iron map of the ACP tissue block shows a very diffuse iron load, with mean
6 iron values of 2.57 ± 1.45 mM, in the putamen, which is about 50% lower than our recent
7 magnetometry study which quantified ferritin-iron in the same structure of the same patient⁶⁵. This is
8 likely due to the combination of very fast relaxation times and the lack of an appropriate ROR in the
9 slice. In contrast to AD and HD, iron accumulation in ACP is directly related to its genetic
10 background, and results from the absence of functioning ceruloplasmin¹³. The lack of ceruloplasmin-
11 mediated oxidation of ferrous iron (Fe^{2+}) to ferric iron (Fe^{3+}) impairs iron efflux from astrocytes, and
12 leads to massive iron accumulation within these cells, while neurons that are mainly dependent on the
13 supply of iron from astrocytes are probably iron-starved^{13,66}. Although ferritin-bound iron appears to
14 be by far the most abundant iron form in the aceruloplasminemia brain^{65,67,68}, these observations are
15 based on patients with end-stage aceruloplasminemia, and it remains unclear how the increase in
16 either total iron levels, as suggested by previous R_2^* ^{13,69,70}, and QSM studies⁶⁹, or in the amount of
17 ferritin-bound iron, are associated with the clinical course of the disease. The apparent contradiction
18 with the weak ferritin staining for the tissue block can perhaps be resolved by considering that the
19 long formalin fixation (~ 5 years) can impact the tissue quality and staining efficiency.

20 Different MRI methods, in addition to those already mentioned, have been used to estimate the effect
21 of ferritin nanoparticles on the MRI parameters. In fact, ferritin-bound iron has long been identified as
22 the main source of iron-driving contrast, given the large abundance of the protein in the brain and its
23 magnetic properties. The magnetic susceptibility of a single ferritin protein was estimated as $\chi = 520$
24 ppm for a fully loaded particle¹⁹, although this value might be an upper limit^{18,71}.

25 Ferritin-iron displays a peculiar linear inverse dependence of T_2 with B_0 field⁷², a trend that is retained
26 in brain tissue and is attributed to the ‘fingerprint’ of iron stores. This characteristic is exploited by the
27 Field Dependent Transverse Relaxation Rate Increase (FDRI) metrics⁷³.

28 A method based on direct saturation to sensitize image contrast based on iron load⁷⁴ has demonstrated
29 a linear relation with the tissue iron content and an improved gray matter-white matter contrast with
30 respect to T_2 -weighted images. The ORS method here proposed differs in the acquisition protocol,
31 with a much larger ORS frequency range being probed here, and in the data post-processing.

32

33 When inspecting the ferritin-bound iron maps, some caveats should be considered. Firstly, our method
34 assumes that the only source of contrast are ferritin nanoparticles carrying ferrihydrite in the core.
35 This is a simplification, as ferrihydrite is probably also included in hemosiderin⁷⁵. Also,
36 magnetite/maghemite is located in the brain either outside or within ferritin^{16,76}. Recent studies,

1 though, have shown that these additional minerals are approximately three orders of magnitude less
2 abundant than ferritin-bound iron.^{55,56}

3 Secondly, we assumed that the iron loading of each ferritin protein was approximately equal to half of
4 the maximum filling capacity of the homonymous protein, while lower iron loading ranges, i. e.
5 between 1500-1850 iron ions within each ferritin protein, have been reported for AD brain tissue and
6 controls⁷⁷. However, since the magnetization of the ferritin particle would not, or only minimally,
7 depend on the iron loading, this does not significantly affect the total ferritin-iron concentrations
8 reported here.

9 Additionally, the ferritin-bound iron maps were obtained from contrast maps that were referenced to a
10 region (ideally) without iron. Therefore, the iron concentrations here displayed cannot be considered
11 as absolute. This is especially clear in the case of the ACP tissue block, where the ferritin-bound iron
12 map shows comparable iron concentrations to the HD case, despite the striking difference in the
13 Meguro staining. This is probably due to the lack of a good ROR in the ACP tissue block.

14 Finally, T_2 maps (not acquired in this study) can provide additional information on the degree of iron
15 accumulation and, in combination with the T_2^* maps, could offer valuable information on the effective
16 size of iron-rich compartments⁷⁸.

17

18 In conclusion, we adapted an ORS method^{46,39} to quantify the ferritin-bound iron pool in the post-
19 mortem brain tissue of three patients affected by neurological diseases associated with increased brain
20 iron. This method can aid the interpretation of R_2^* and QSM maps, especially when these are
21 confounded by reconstruction artifacts or the co-presence of iron and myelin. The accuracy of the
22 ferritin-bound iron map depends on the availability, within the tissue, of a region without (or with
23 little) iron content with respect to the region of interest. We foresee that this method will find use in
24 the study of the progression of neurodegenerative diseases characterized by brain iron accumulation
25 and the assessment of iron chelation therapy.

26

27 **Author contributions**

28 **Lucia Bossoni:** Conceptualization, Methodology, Software, Investigation, Writing – Original Draft,
29 Visualization, Project Administration; **Ingrid Hegemann-Kleinn:** histological analysis; **Sjoerd van**
30 **Duinen:** supervision of the histological analysis; **Lena H. P. Vroegindewij:** Resources, Writing –
31 Review & Editing; **Janneke G. Langendonk:** Resources, Writing – Review & Editing; **Lydiane**
32 **Hirschler:** Software, Writing – Review & Editing; **Andrew G. Webb:** Methodology, Resources,
33 Writing – Review & Editing; **Louise van der Weerd:** Methodology, Resources, Writing – Review &
34 Editing.

35 **Acknowledgements**

1 The authors are grateful to E. Suidgeest, E. Ercan and M. Bulk for assistance in the lab and useful
2 discussions.

4 Funding

5 This study was supported by the Netherlands Organization for Scientific Research (NWO) through a
6 VENI fellowship to L.B. (0.16.Veni.188.040).

9 **Declarations of interest:** none.

10 Tables

11 **Table 1.** Summary of the acquisition parameters for the MGE sequence, with eight echoes (N_{echo}). TE_1
12 refers to the first echo time, ΔTE refers to the inter-echo time. TR is the recovery time and FA the flip
13 angle. Abbreviations: *HD*: Huntington's disease, *ACP*: aceruloplasminemia, *AD*: Alzheimer's
14 disease.

Sample	Pixel size (mm ³)	FA (degrees)	Averages	TR (ms)	TE ₁ (ms)	N _{echo}	ΔTE	Total scan time
HD	(0.15) ³	25	20	107.3	5.2	8	4.34	3h26m
ACP	(0.15) ³	25	20	130.4	1.96	8	2.21	3h55m
AD	(0.15) ³	25	20	107.3	5.2	8	4.34	3h26m

15

16 **Table 2.** Summary of the acquisition parameters for the ORS-SSFP acquisition. Symbols: *BW*: ORS
17 Pulse bandwidth; ν_0 : frequency of the off-resonance saturation pulse; $\Delta\nu_0$: interval between ORS
18 frequencies, *HD*: Huntington's disease, *ACP*: aceruloplasminemia, *AD*: Alzheimer's disease.

Sample	BW [Hz]	ν_0 range [Hz]	$\Delta\nu_0$ [Hz]	Total scan time	Pixel size (mm ³)	Reference for contrast calculation (ROR)
Phantom	500	250-649	7	1.3h	0.3x0.3x2	Agar-only compartment
HD	500	250-700	5	~8h10min	0.15x0.15x2	Internal capsule
ACP	500	250-700	5	~8h10min	0.15x0.15x2	Internal Capsule
AD	500	250-700	5	~8h10min	0.15x0.15x2	Cortical white matter

19

20

1 **Figure Captions**

2

3 **Figure 1. Analysis pipeline.**

4 *After the acquisition of the non-saturated images ('control'), the saturated images are acquired, and*
5 *the ORS image is derived. The Z-spectrum is shown, but was not used in the analysis. The region of*
6 *reference (ROR) is shown here as a white dotted line in the bottom row. The contrast maps are*
7 *obtained from the ORS image and the mean intensity in the ROR, and fitted to the model discussed*
8 *below. An example of the fit is shown in the right panel. The fit is the red solid line overlapped on to*
9 *the experimental data (blue squares). Finally, a map of iron concentration in mM is obtained ($[Fe]_{ORS}$*
10 *map).*

11

12 **Figure 2. Validation on a ferritin phantom.** *Panel A shows the control image with the nominal iron*
13 *concentration in mM, per compartment. Panel B shows the ferritin-bound iron map in mM, as*
14 *obtained with the ORS sequence and the fitting method discussed above. The bright outer rim in the*
15 *iron map is likely caused by B_1 inhomogeneities, since a linear eight-leg birdcage coil with a high*
16 *filling factor was employed. Panel C shows a comparison between the nominal iron concentration*
17 *and the fitted one from the method discussed in this work. Blue data with error bars represent the*
18 *mean and standard deviation of the iron concentration in the ROI drawn in each sample*
19 *compartment. The red solid line is the identity line and the dashed lines account for the spread in iron*
20 *loading as reported in literature for horse spleen ferritin from the same producer. Panel D is the*
21 *Bland-Altman plot of the same data. The black-solid line is the line of equality. The blue line is the*
22 *bias. The dashed lines enclosing the green area are the limits of agreement. The dotted lines mark the*
23 *95% confidence intervals for each estimated statistical quantity.*

24

25 **Figure 3. Comparison of the quantitative MRI and histological methods to assess tissue iron load**
26 **on the Alzheimer tissue block:** *Top row: MRI R_2^* , QSM and ferritin-bound iron mapping. Bottom*
27 *row: histological staining for myelin, iron (Perl's and Meguro) and ferritin, Scalebar: 5 mm. The 4th*
28 *echo of the MGE image is shown for anatomical reference. The pink circle in the MGE image*
29 *encloses the region of reference (ROR). The panel on the right shows the result of the linear*
30 *regression analysis between the ROI mean intensity of $[Fe]_{ORS}$ map and the histological staining for*
31 *iron. The Pearson's correlation coefficient and p-value are reported on the graph.*

32

1 **Figure 4. Comparison of the quantitative MRI and histological methods to assess tissue iron load**
2 **in the Huntington's diseases tissue block (labels as above):** Scalebar: 5 mm. Abbreviations: IC=
3 internal capsule, PU=putamen, CN=caudate nucleus. The MGE image displays the third echo.

4

5 **Figure 5. Comparison of the quantitative MRI and histological methods to assess tissue iron load**
6 **on the aceruloplasminemia tissue block (labels as above):** Scalebar: 5 mm. Abbreviations: IC=
7 internal capsule, PU=putamen, CN=caudate nucleus, GP=globus pallidus. The MGE image displays
8 the first echo.

9

10 **References**

- 11 1. Hallgren B, Sourander P. the Effect of Age on the Non-Haemin Iron in the Human Brain. *J*
12 *Neurochem.* 1958;3(1):41-51. doi:10.1111/j.1471-4159.1958.tb12607.x
- 13 2. Ward RJ, Zucca FA, Duyn JH, Crichton RR, Zecc L. The role of iron in brain ageing and
14 neurodegenerative disorders. *Lancet Neurol.* 2014;13(10):1045-1060. doi:10.1016/S1474-
15 4422(14)70117-6
- 16 3. Zecca L, Youdim MBH, Riederer P, Connor JR, Crichton RR. Iron, brain ageing and
17 neurodegenerative disorders. *Nat Rev Neurosci.* 2004;5(11):863-873. doi:10.1038/nrn1537
- 18 4. Li K, Reichmann H. Role of iron in neurodegenerative diseases. *J Neural Transm.*
19 2016;123(4):389-399. doi:10.1007/s00702-016-1508-7
- 20 5. Daugherty AM, Raz N. Appraising the Role of Iron in Brain Aging and Cognition: Promises and
21 Limitations of MRI Methods. *Neuropsychol Rev.* 2015;25(3):272-287. doi:10.1007/s11065-
22 015-9292-y
- 23 6. Harman D. Aging: a theory based on free radical and radiation chemistry. *J Gerontol.*
24 1956;11(3):298-300. doi:10.1093/geronj/11.3.298
- 25 7. Ashraf A, Clark M, So PW. The aging of iron man. *Front Aging Neurosci.* 2018;10(MAR):1-23.
26 doi:10.3389/fnagi.2018.00065
- 27 8. Stockwell BR, Friedmann Angeli JP, Bayir H, et al. Ferroptosis: A Regulated Cell Death Nexus
28 Linking Metabolism, Redox Biology, and Disease. *Cell.* 2017;171(2):273-285.
29 doi:10.1016/j.cell.2017.09.021

- 1 9. Angeli JPF, Shah R, Pratt DA, Conrad M. Ferroptosis Inhibition: Mechanisms and
2 Opportunities. *Trends Pharmacol Sci*. 2017;38(5):489-498. doi:10.1016/j.tips.2017.02.005
- 3 10. Ong W, Farooqui AA. Iron , neuroinflammation , and Alzheimer ' s disease. 2005;8:183-200.
- 4 11. Rivera-Mancía S, Pérez-Neri I, Ríos C, Tristán-López L, Rivera-Espinosa L, Montes S. The
5 transition metals copper and iron in neurodegenerative diseases. *Chem Biol Interact*.
6 2010;186(2):184-199. doi:10.1016/j.cbi.2010.04.010
- 7 12. Rosas HD, Chen YI, Doros G, et al. Alterations in brain transition metals in Huntington disease:
8 An evolving and intricate story. *Arch Neurol*. 2012;69(7):887-893.
9 doi:10.1001/archneurol.2011.2945
- 10 13. Miyajima H. Aceruloplasminemia. *Neuropathology*. 2015;35(1):83-90.
11 doi:10.1111/neup.12149
- 12 14. Finazzi D, Arosio P. Biology of ferritin in mammals: an update on iron storage, oxidative
13 damage and neurodegeneration. *Arch Toxicol*. 2014;88(10):1787-1802. doi:10.1007/s00204-
14 014-1329-0
- 15 15. Arosio P, Elia L, Poli M. Ferritin, cellular iron storage and regulation. *IUBMB Life*.
16 2017;69(6):414-422. doi:10.1002/iub.1621
- 17 16. Quintana C, Gutiérrez L. Could a dysfunction of ferritin be a determinant factor in the
18 aetiology of some neurodegenerative diseases? *Biochim Biophys Acta - Gen Subj*.
19 2010;1800(8):770-782. doi:10.1016/j.bbagen.2010.04.012
- 20 17. Schenck JF, Zimmerman EA. High-field magnetic resonance imaging of brain iron: Birth of a
21 biomarker? *NMR Biomed*. 2004;17(7):433-445. doi:10.1002/nbm.922
- 22 18. Makhlof SA, Parker FT, Berkowitz AE. Magnetic hysteresis anomalies in ferritin. *Phys Rev B*.
23 1997;55(22):R14717-R14720. doi:10.1103/PhysRevB.55.R14717
- 24 19. Schenck JF. Health and Physiological Effects of Human Exposure to Whole-Body Four-Tesla
25 Magnetic Fields during MRI. *Ann N Y Acad Sci*. 1992;649(1 Biological Ef):285-301.
26 doi:10.1111/j.1749-6632.1992.tb49617.x
- 27 20. Salgado JC, Olivera-Nappa A, Gerdtzen ZP, et al. Mathematical modeling of the dynamic
28 storage of iron in ferritin. *BMC Syst Biol*. 2010;4. doi:10.1186/1752-0509-4-147
- 29 21. Kakhlon O, Gruenbaum Y, Cabantchik ZL. Repression of ferritin expression increases the labile

- 1 iron pool, oxidative stress, and short-term growth of human erythroleukemia cells. *Blood*.
2 2001;97(9):2863-2871. doi:10.1182/blood.V97.9.2863
- 3 22. Ghassaban K, Liu S, Jiang C, Haacke EM. Quantifying iron content in magnetic resonance
4 imaging. *Neuroimage*. 2019;187(October 2017):77-92.
5 doi:10.1016/j.neuroimage.2018.04.047
- 6 23. Chavhan GB, Babyn PS, Thomas B, Shroff MM, Haacke EM. Principles, Techniques, and
7 Applications of T2*-based MR Imaging and Its Special Applications. *Radiogr Educ Exhib*.
8 2009;29(5):1433-1449. doi:10.1148/rg.295095034
- 9 24. Brass SD, Chen NK, Mulkern R V., Bakshi R. Magnetic resonance imaging of iron deposition in
10 neurological disorders. *Top Magn Reson Imaging*. 2006;17(1):31-40.
11 doi:10.1097/01.rmr.0000245459.82782.e4
- 12 25. Bartzokis G, Sultzer D, Mintz J, et al. In vivo evaluation of brain iron in Alzheimer's disease and
13 normal subjects using MRI. *Biol Psychiatry*. 1994;35(7):480-487. doi:10.1016/0006-
14 3223(94)90047-7
- 15 26. Bartzokis G, Lu PH, Tishler TA, et al. Myelin Breakdown and Iron Changes in Huntington's
16 Disease: Pathogenesis and Treatment Implications. *Neurochem Res*. 2007;32(10):1655-1664.
17 doi:10.1007/s11064-007-9352-7
- 18 27. Raven EP, Lu PH, Tishler TA, Heydari P, Bartzokis G. Increased iron levels and decreased tissue
19 integrity in hippocampus of Alzheimer's disease detected in vivo with magnetic resonance
20 imaging. *J Alzheimer's Dis*. 2013;37(1):127-136. doi:10.3233/JAD-130209
- 21 28. Langkammer C, Krebs N, Goessler W, et al. Quantitative MR Imaging of Brain Iron: A
22 Postmortem Validation Study. *Radiology*. 2010;257(2):455-462. doi:10.1148/radiol.10100495
- 23 29. Haacke EM, Cheng NYC, House MJ, et al. Imaging iron stores in the brain using magnetic
24 resonance imaging. *Magn Reson Imaging*. 2005;23(1):1-25. doi:10.1016/j.mri.2004.10.001
- 25 30. Langkammer C, Schweser F, Krebs N, et al. NeuroImage Quantitative susceptibility mapping (
26 QSM) as a means to measure brain iron ? A post mortem validation study. 2012;62:1593-
27 1599. doi:10.1016/j.neuroimage.2012.05.049
- 28 31. Eskreis-Winkler S, Zhang Y, Zhang J, et al. The clinical utility of QSM: disease diagnosis,
29 medical management, and surgical planning. *NMR Biomed*. 2017;30(4).
30 doi:10.1002/nbm.3668

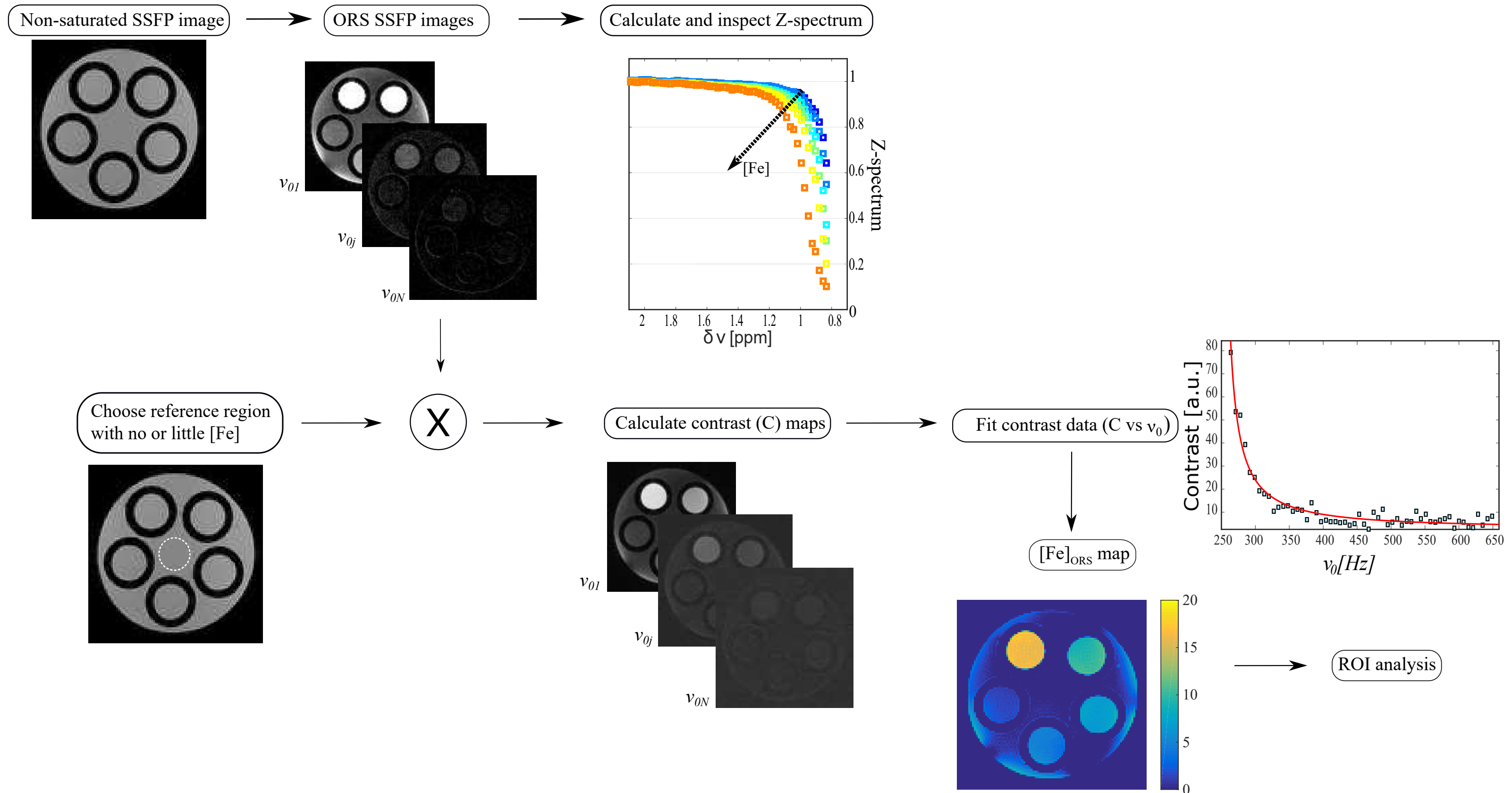
- 1 32. Hametner S, Endmayr V, Deistung A, et al. The influence of brain iron and myelin on magnetic
2 susceptibility and effective transverse relaxation - A biochemical and histological validation
3 study. *Neuroimage*. 2018;179(February):117-133. doi:10.1016/j.neuroimage.2018.06.007
- 4 33. Li T-Q, Yao B, van Gelderen P, et al. Characterization of T(2)* heterogeneity in human brain
5 white matter. *Magn Reson Med*. 2009;62(6):1652-1657. doi:10.1002/mrm.22156
- 6 34. Stüber C, Morawski M, Schäfer A, et al. Myelin and iron concentration in the human brain: A
7 quantitative study of MRI contrast. *Neuroimage*. 2014;93:95-106.
8 doi:10.1016/j.neuroimage.2014.02.026
- 9 35. Wharton S, Bowtell R. Fiber orientation-dependent white matter contrast in gradient echo
10 MRI. *Proc Natl Acad Sci U S A*. 2012;109(45):18559-18564. doi:10.1073/pnas.1211075109
- 11 36. Möller HE, Bossoni L, Connor JR, et al. Iron , Myelin , and the Brain : Neuroimaging Meets
12 Neurobiology. *Trends Neurosci*. 42(6):384-401. doi:10.1016/j.tins.2019.03.009
- 13 37. Tanimoto A, Oshio K, Suematsu M, Pouliquen D, Stark DD. Relaxation effects of clustered
14 particles. *J Magn Reson Imaging*. 2001;14(1):72-77. doi:10.1002/jmri.1153
- 15 38. Gossuin Y, Gillis P, Muller RN, Hocq A. Relaxation by clustered ferritin: A model for ferritin-
16 induced relaxation in vivo. *NMR Biomed*. 2007;20(8):749-756. doi:10.1002/nbm.1140
- 17 39. Zurkiya O, Hu X. Off-resonance saturation as a means of generating contrast with
18 superparamagnetic nanoparticles. *Magn Reson Med*. 2006;56(4):726-732.
19 doi:10.1002/mrm.21024
- 20 40. Delangre S, Vuong QL, Henrard D, Po C, Gallez B, Gossuin Y. Bottom-up study of the MRI
21 positive contrast created by the Off-Resonance Saturation sequence. *J Magn Reson*.
22 2015;254:98-109. doi:10.1016/j.jmr.2015.02.014
- 23 41. Jian N, Dowle M, Horniblow RD, Tselepis C, Palmer RE. Morphology of the ferritin iron core by
24 aberration corrected scanning transmission electron microscopy. *Nanotechnology*.
25 2016;27(46):46LT02. doi:10.1088/0957-4484/27/46/46LT02
- 26 42. Li W, Avram A V, Wu B, Xiao X, Liu C. Integrated Laplacian-based phase unwrapping and
27 background phase removal for quantitative susceptibility mapping. 2014;(August 2013):219-
28 227. doi:10.1002/nbm.3056
- 29 43. Li W, Wang N, Yu F, et al. A method for estimating and removing streaking artifacts in

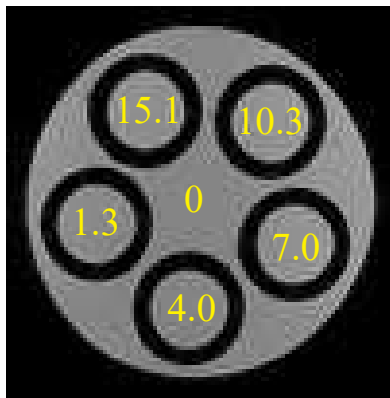
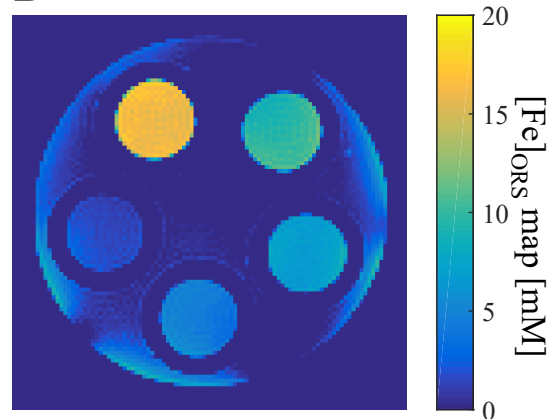
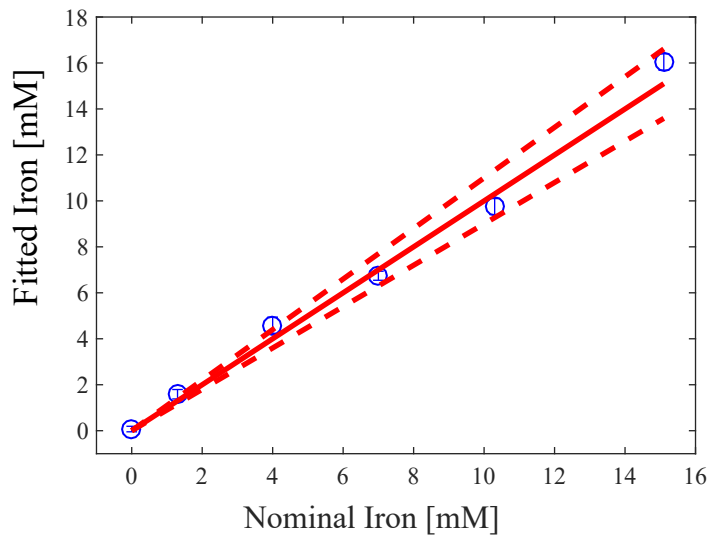
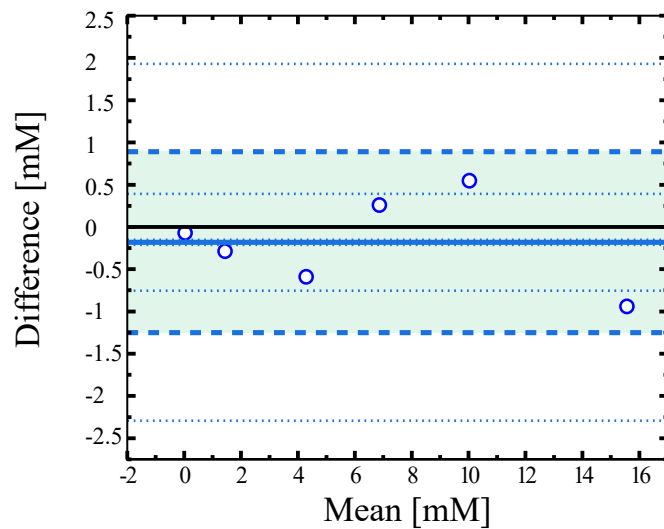
- 1 quantitative susceptibility mapping. *Neuroimage*. 2015;108:111-122.
2 doi:10.1016/j.neuroimage.2014.12.043.A
- 3 44. Zijl P van, Yadav N. Chemical exchange saturation transfer (CEST): what is in a name and what
4 isn't? *Magn Reson Med*. 2011;65(4):927-948. doi:10.1002/mrm.22761.Chemical
- 5 45. Vuong QL, Berret JF, Fresnais J, Gossuin Y, Sandre O. A universal scaling law to predict the
6 efficiency of magnetic nanoparticles as MRI T2-contrast agents. *Adv Healthc Mater*.
7 2012;1(4):502-512. doi:10.1002/adhm.201200078
- 8 46. Delangre S, Vuong QL, Po C, Gallez B, Gossuin Y. Improvement of the Off-Resonance
9 Saturation, an MRI sequence for positive contrast with SPM particles: Theoretical and
10 experimental study. *J Magn Reson*. 2016;265:99-107. doi:10.1016/j.jmr.2016.02.002
- 11 47. Matt A. Bernstein, Kevin F. King XJZ. *Handbook of MRI Pulse Sequences.*; 2004.
12 doi:10.4314/bcse.v21i3.21211
- 13 48. van Duijn S, Nabuurs RJA, van Duinen SG, Natté R. Comparison of histological techniques to
14 visualize iron in paraffin-embedded brain tissue of patients with Alzheimer's disease. *J*
15 *Histochem Cytochem*. 2013;61(11):785-792. doi:10.1369/0022155413501325
- 16 49. Bland DGA and JM. Measurement in Medicine : The Analysis of Method Comparison Studies
17 Author (s): D . G . Altman and J . M . Bland Published by : Blackwell Publishing for the Royal
18 Statistical Society Stable URL : <http://www.jstor.org/stable/2987937>. 2008;32(3):307-317.
- 19 50. Giavarina D. Understanding Bland Altman analysis. *Biochem Medica*. 2015;25(2):141-151.
20 doi:10.11613/BM.2015.015
- 21 51. Bulk M, Abdelmoula WM, Geut H, et al. Quantitative MRI and laser ablation-inductively
22 coupled plasma-mass spectrometry imaging of iron in the frontal cortex of healthy controls
23 and Alzheimer's disease patients. *Neuroimage*. 2020;215(April):116808.
24 doi:10.1016/j.neuroimage.2020.116808
- 25 52. Damulina A, Pirpamer L, Soellradl M, et al. Cross-sectional and Longitudinal Assessment of
26 Brain Iron Level in Alzheimer Disease Using 3-T MRI. *Radiology*. 2020;(15):192541.
27 doi:10.1148/radiol.2020192541
- 28 53. Bulk M, Kenkhuis B, Van Der Graaf LM, Goeman JJ, Natté R, Van Der Weerd L. Postmortem
29 T2*-Weighted MRI Imaging of Cortical Iron Reflects Severity of Alzheimer's Disease. *J*
30 *Alzheimer's Dis*. 2018;65(4):1125-1137. doi:10.3233/JAD-180317

- 1 54. van Bergen JMG, Li X, Hua J, et al. Colocalization of cerebral iron with Amyloid beta in Mild
2 Cognitive Impairment. *Sci Rep*. 2016;6(March):35514. doi:10.1038/srep35514
- 3 55. van der Weerd L, Lefering A, Webb A, et al. Effects of Alzheimer's disease and formalin
4 fixation on the different mineralised-iron forms in the human brain. *Sci Rep*.
5 2020;10(16440):2020.06.02.129593. doi:10.1101/2020.06.02.129593
- 6 56. Bulk M, van der Weerd L, Breimer W, et al. Quantitative comparison of different iron forms in
7 the temporal cortex of Alzheimer patients and control subjects. *Sci Rep*. 2018;8(1):6898.
8 doi:10.1038/s41598-018-25021-7
- 9 57. Tao Y, Wang Y, Rogers JT, Wang F. Perturbed iron distribution in Alzheimer's disease serum,
10 cerebrospinal fluid, and selected brain regions: A systematic review and meta-analysis. *J*
11 *Alzheimer's Dis*. 2014;42(2):679-690. doi:10.3233/JAD-140396
- 12 58. House MJ, St. Pierre TG, McLean C. 1.4T study of proton magnetic relaxation rates, iron
13 concentrations, and plaque burden in Alzheimer's disease and control postmortem brain
14 tissue. *Magn Reson Med*. 2008;60(1):41-52. doi:10.1002/mrm.21586
- 15 59. Xiaojun Yu, MS Tingting Du, MS Ning Song, PhD Qing He, MS Yong Shen, PhD Hong Jiang, PhD
16 Junxia Xie P. Decreased iron levels in the temporal cortex in postmortem human brains with
17 Parkinson disease. *Neurology*. 2013;80(5):492-495.
18 doi:10.1212/01.wnl.0000435455.95141.16
- 19 60. Bartzokis G, Cummings J, Perlman S, Hance DB, Mintz J. Increased basal ganglia iron levels in
20 Huntington disease. *Arch Neurol*. 1999;56(5):569-574. doi:10.1001/archneur.56.5.569
- 21 61. Domínguez D JF, Ng ACL, Poudel G, et al. Iron accumulation in the basal ganglia in
22 Huntington's disease: Cross-sectional data from the IMAGE-HD study. *J Neurol Neurosurg*
23 *Psychiatry*. 2016;87(5):545-549. doi:10.1136/jnnp-2014-310183
- 24 62. Jurgens CK, Jasinschi R, Ekin A et al. MRI T2 hypointensities in basal ganglia of premanifest
25 Huntington's disease. *Plos Curr Huntingt Dis*. 2010;(2:RNN1173).
- 26 63. Jiri M.G. van Bergen, MSc, Jun Hua, PhD, Paul G. Unschuld, MD IAL, Lim, PhD, Craig K. Jones,
27 PhD, Russell L. Margolis, MD, Christopher A. Ross M, PhD, Peter C.M. van Zijl, PhD, and Xu Li
28 P. Quantitative susceptibility mapping suggests altered brain iron in premanifest Huntington's
29 disease. *AJNR Am J Neuroradiol*. 2016;5(37):789-796. doi:10.3174/ajnr.A4617.Quantitative
- 30 64. Sánchez-Castañeda C, Squitieri F, Di Paola M, Dayan M, Petrollini M, Sabatini U. The role of

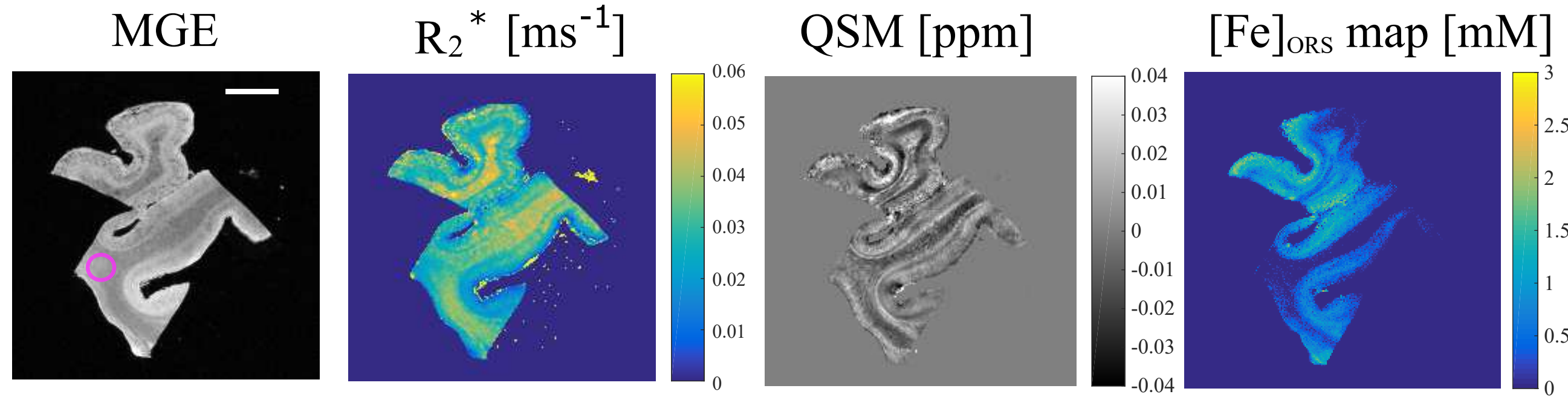
- 1 iron in gray matter degeneration in huntington's disease: A magnetic resonance imaging
2 study. *Hum Brain Mapp.* 2015;36(1):50-66. doi:10.1002/hbm.22612
- 3 65. Vroegindeweyj, Lena H.P., Lucia Bossoni AJWB, Wilson JHP, Bulk M, et al. Quantification of
4 different iron forms in the aceruloplasminemia brain to explore iron-related
5 neurodegeneration. *medRxiv.* 2020. <https://doi.org/10.1101/2020.10.15.20206102>.
- 6 66. Jeong SY, David S. Age-Related Changes in Iron Homeostasis and Cell Death in the Cerebellum
7 of Ceruloplasmin-Deficient Mice. 2006;26(38):9810-9819. doi:10.1523/JNEUROSCI.2922-
8 06.2006
- 9 67. Kaneko K, Hineno A, Yoshida K. Extensive brain pathology in a patient with
10 aceruloplasminemia with a prolonged duration of illness. *Hum Pathol.* 2012;43(3):451-456.
11 doi:10.1016/j.humphath.2011.05.016
- 12 68. K. Kaneko, K. Yoshida KA et al. Astrocytic Deformity and Globular Structures Are
13 Characteristic of the Brains of Patients with Aceruloplasminemia. *J Neuropathol Exp Neurol.*
14 2002;61(12):1069-1077.
- 15 69. Zhou L, Chen Y, Li Y, et al. Intracranial iron distribution and quantification in
16 aceruloplasminemia: A case study. *Magn Reson Imaging.* 2020;70(December 2019):29-35.
17 doi:10.1016/j.mri.2020.02.016
- 18 70. Shang H-F. Desferrioxamine Treatment of Aceruloplasminemia: Long-term Follow-up. *Mov*
19 *Disord.* 2011;26(11):2131-2147. doi:10.1002/mds.23768
- 20 71. Brooks RA, Vymazal J, Goldfarb RB, Bulte JWM, Aisen P. Relaxometry and Magnetometry of
21 Ferritin. *Magn Reson Med.* 1998;(40):227-235.
- 22 72. Brooks RA, Vymazal J, Bulte JW, Baumgarner CD, Tran V. Comparison of T2 relaxation in
23 blood, brain, and ferritin. *J Magn Reson Imaging.* 1995;5(4):446-450.
24 doi:10.1002/jmri.1880050414
- 25 73. Bartzokis G, Aravagiri M, Oldendorf WH, Mintz J, Marder SR. Field dependent transverse
26 relaxation rate increase may be a specific measure of tissue iron stores. *Magn Reson Med.*
27 1993;29(4):459-464. doi:10.1002/mrm.1910290406
- 28 74. Smith SA, Bulte JWM, van Zijl PCM. Direct saturation MRI: Theory and application to imaging
29 brain iron. *Magn Reson Med.* 2009;62(2):384-393. doi:10.1002/mrm.21980

- 1 75. Duyn JH, Schenck J. Contributions to magnetic susceptibility of brain tissue. *NMR Biomed.*
2 2017;30(4):1-37. doi:10.1002/nbm.3546
- 3 76. Kirschvink JL, Kobayashi-Kirschvink a, Woodford BJ. Magnetite biomineralization in the
4 human brain. *Proc Natl Acad Sci U S A.* 1992;89(August):7683-7687.
5 doi:10.1073/pnas.89.16.7683
- 6 77. Dedman DJ, Treffry a, Candy JM, et al. Iron and aluminium in relation to brain ferritin in
7 normal individuals and Alzheimer's-disease and chronic renal-dialysis patients. *Biochem J.*
8 1992;287 (Pt 2:509-514.
9 [http://www.pubmedcentral.nih.gov/articlerender.fcgi?artid=1133194&tool=pmcentrez&ren](http://www.pubmedcentral.nih.gov/articlerender.fcgi?artid=1133194&tool=pmcentrez&rendertype=abstract)
10 [dertype=abstract](http://www.pubmedcentral.nih.gov/articlerender.fcgi?artid=1133194&tool=pmcentrez&rendertype=abstract).
- 11 78. Lee H, Baek SY, Chun SY, Lee JH, Cho HJ. Specific visualization of neuromelanin-iron complex
12 and ferric iron in the human post-mortem substantia nigra using MR relaxometry at 7T.
13 *Neuroimage.* 2018;172(November 2017):874-885. doi:10.1016/j.neuroimage.2017.11.035
- 14

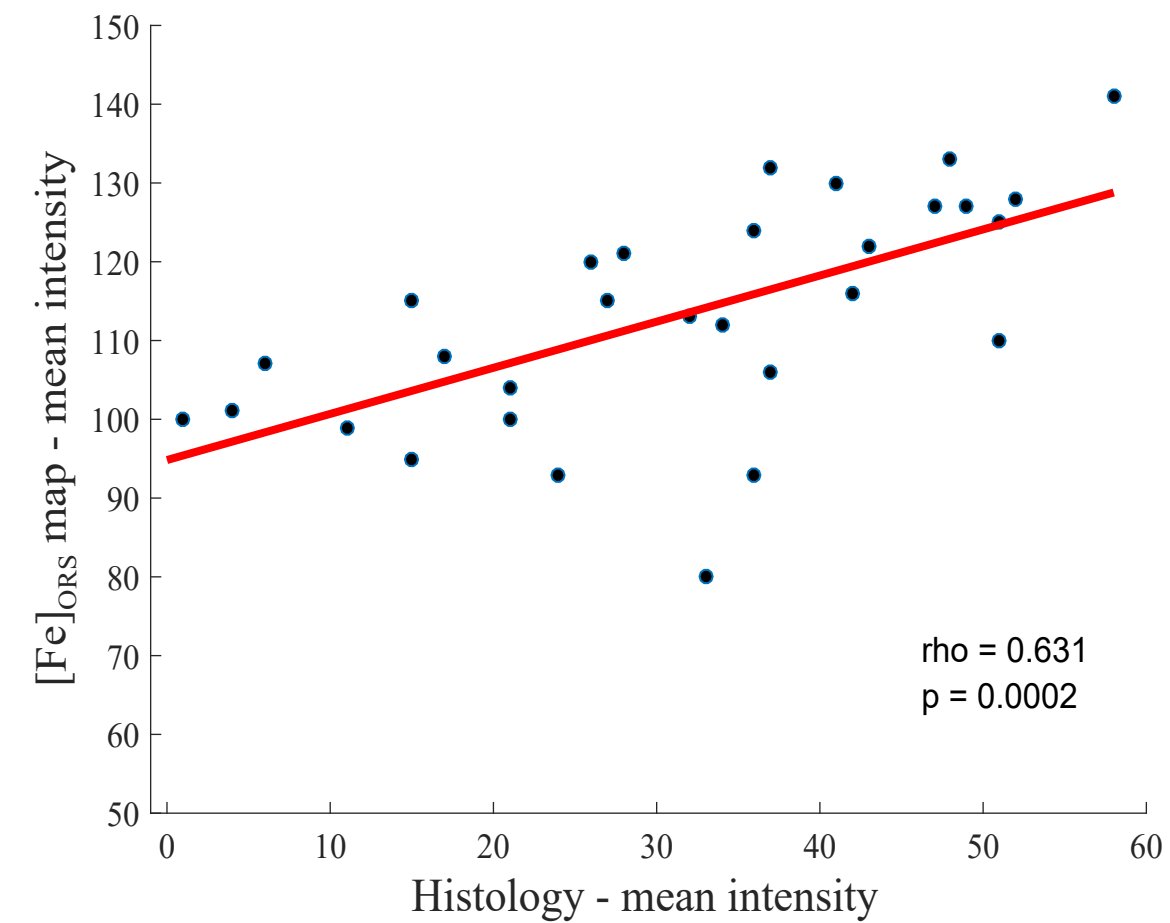
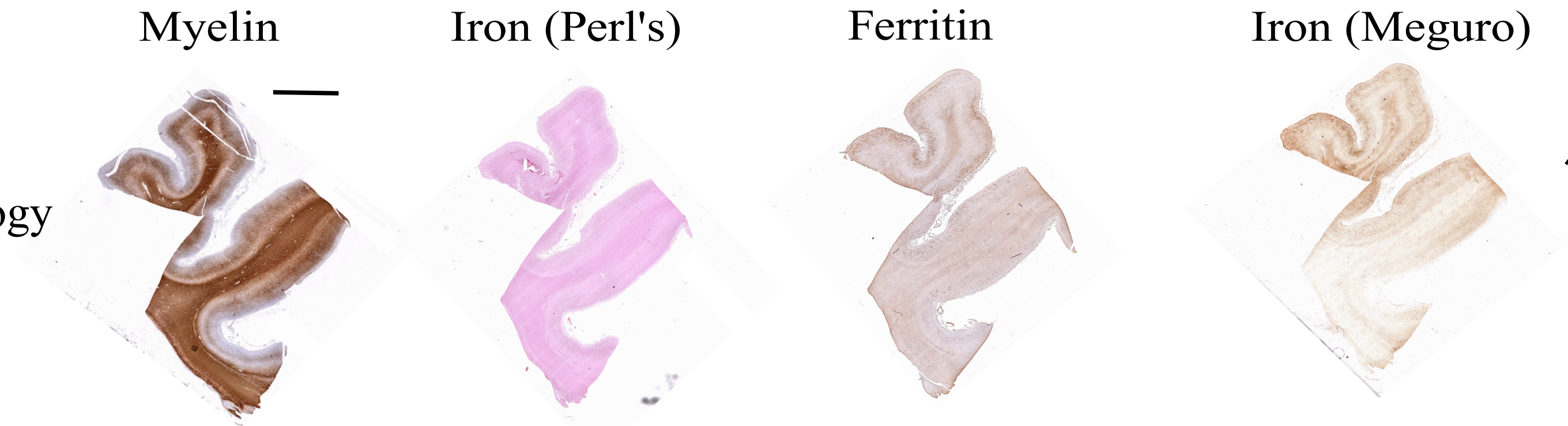


A**B****C****D**

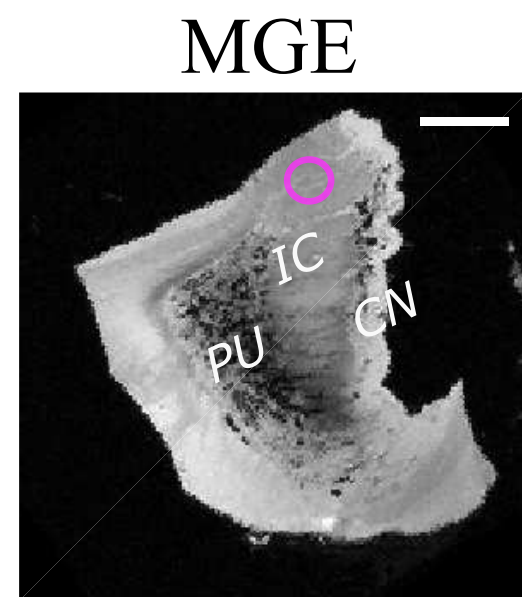
MRI



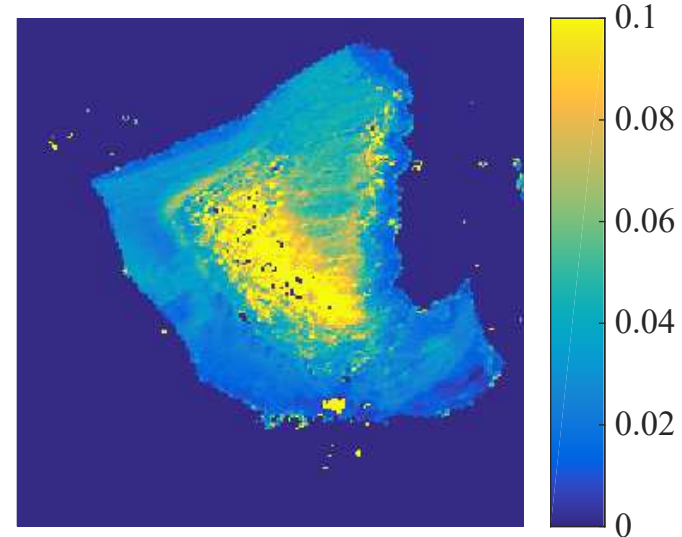
Histology



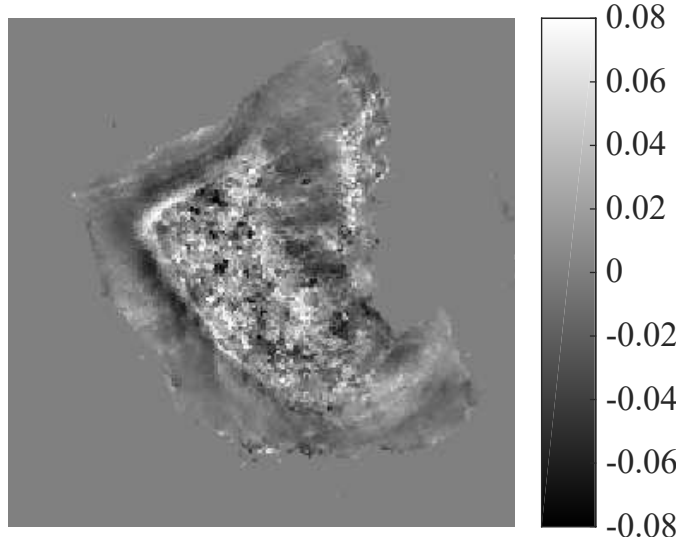
MRI



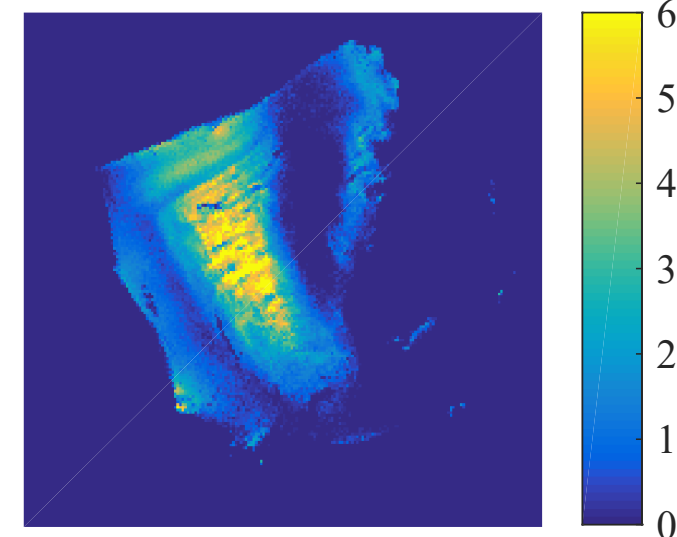
R_2^* [ms^{-1}]



QSM [ppm]

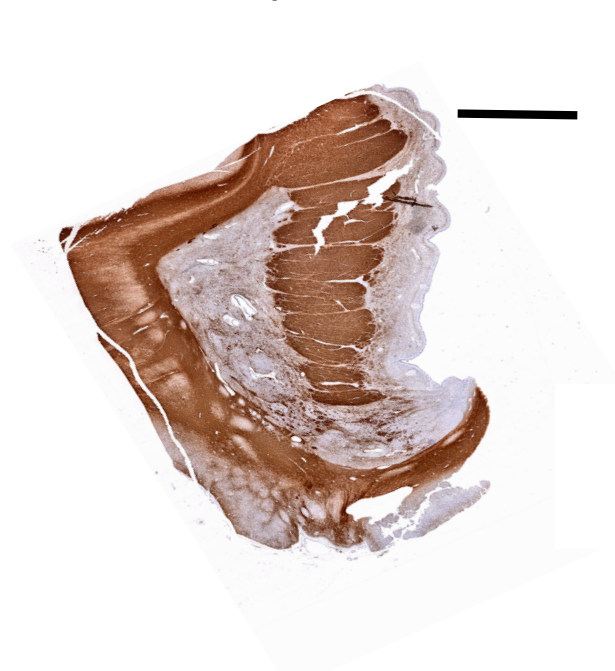


$[\text{Fe}]_{\text{ORS}}$ map [mM]



Histology

Myelin



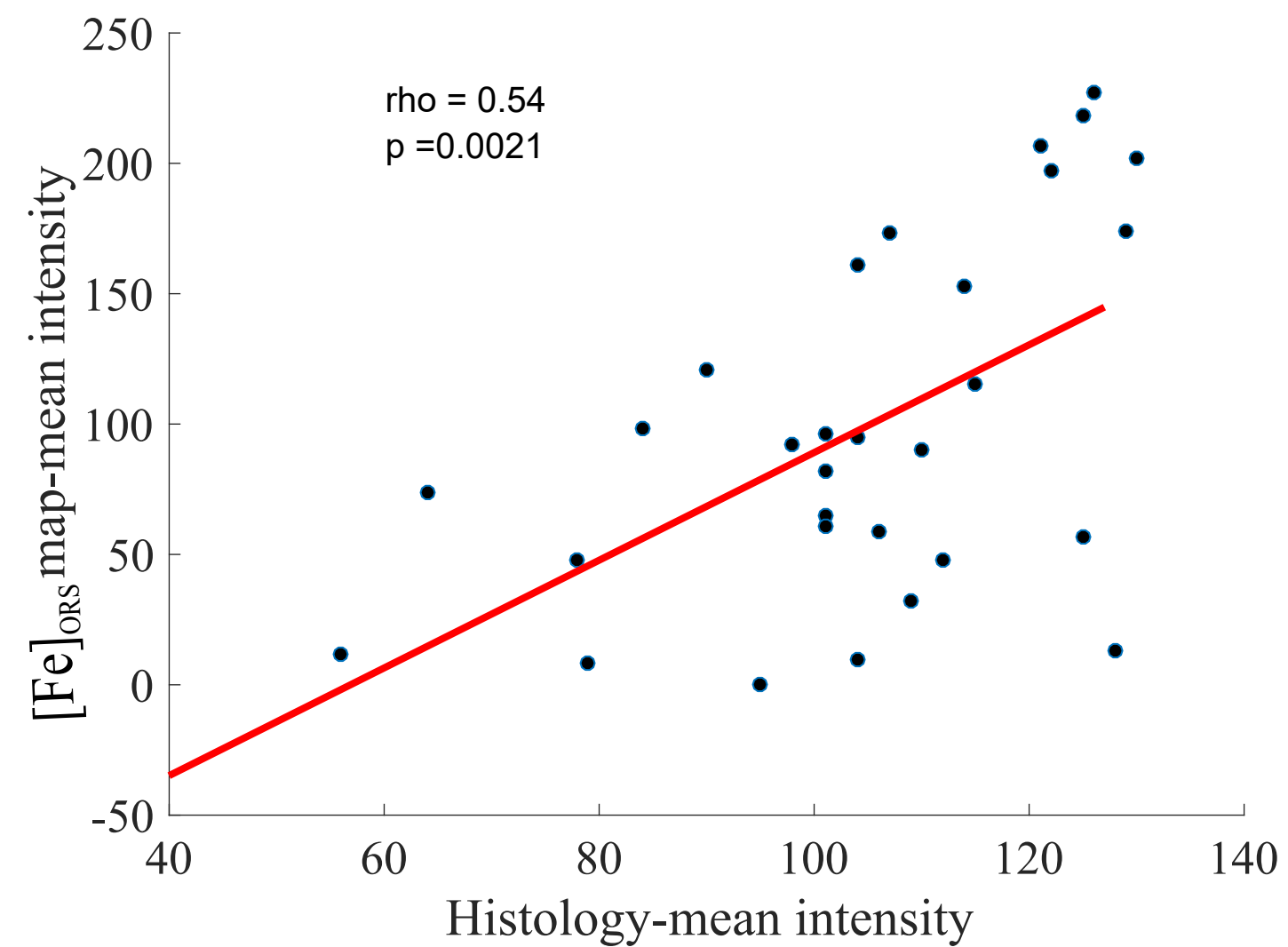
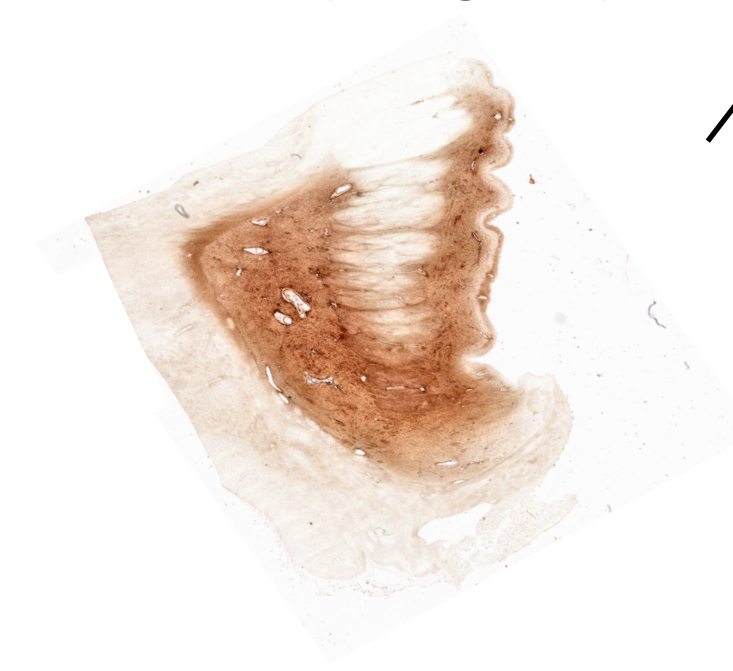
Iron (Perl's)



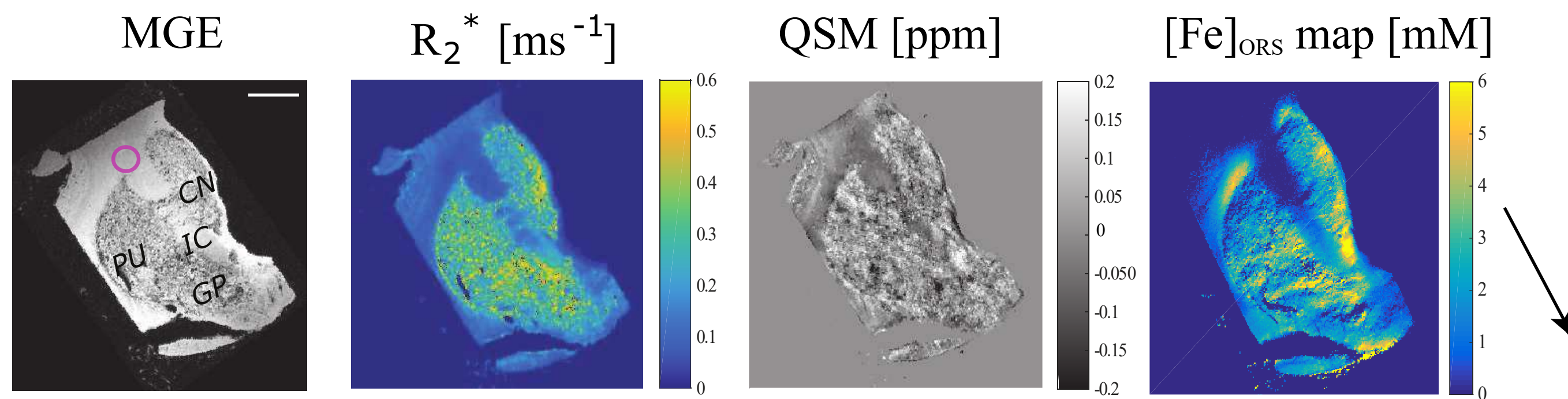
Ferritin



Iron (Meguro)



MRI



Histology

